

Ultrahigh-resolution, high-speed, Fourier domain optical coherence tomography and methods for dispersion compensation

^{1,3}Maciej Wojtkowski, ¹Vivek J. Srinivasan, ¹Tony H. Ko, ¹James G. Fujimoto,
²Andrzej Kowalczyk, ³Jay S. Duker

¹Department of Electrical Engineering and Computer Science and Research Laboratory of Electronics
Massachusetts Institute of Technology, Cambridge, MA 02139

²Institute of Physics, Nicholas Copernicus University, ul. Grudziadzka 5/7, Pl- 87-100 Torun, Poland
³New England Eye Center, Tufts-New England Medical Center, Boston, Massachusetts
maciejw@mit.edu

Abstract: Ultrahigh-resolution optical coherence tomography uses broadband light sources to achieve axial image resolutions on the few micron scale. Fourier domain detection methods enable more than an order of magnitude increase in imaging speed and sensitivity, thus overcoming the sensitivity limitations inherent in ultrahigh-resolution OCT using standard time domain detection. Fourier domain methods also provide direct access to the spectrum of the optical signal. This enables automatic numerical dispersion compensation, a key factor in achieving ultrahigh image resolutions. We present ultrahigh-resolution, high-speed Fourier domain OCT imaging with an axial resolution of 2.1 μm in tissue and 16,000 axial scans per second at 1024 pixels per axial scan. Ultrahigh-resolution spectral domain OCT is shown to provide a \sim 100x increase in imaging speed when compared to ultrahigh-resolution time domain OCT. *In vivo* imaging of the human retina is demonstrated. We also present a general technique for automatic numerical dispersion compensation, which is applicable to spectral domain as well as swept source embodiments of Fourier domain OCT.

©2004 Optical Society of America

OCIS codes: (170.4500) Optical coherence tomography, (170.3880) Medical and biological imaging, (140.3510)

References and Links

1. D. Huang, E. A. Swanson, C. P. Lin, J. S. Schuman, W. G. Stinson, W. Chang, M. R. Hee, T. Flotte, K. Gregory, C. A. Puliafito, and J. G. Fujimoto, "Optical coherence tomography," *Science* **254**, 1178-1181 (1991).
 2. J. G. Fujimoto, "Optical coherence tomography for ultrahigh resolution *in vivo* imaging," *Nat. Biotechnol.* **21**, 1361-1367 (2003).
 3. W. Drexler, U. Morgner, F. X. Kartner, C. Pitris, S. A. Boppart, X. D. Li, E. P. Ippen, and J. G. Fujimoto, "In vivo ultrahigh-resolution optical coherence tomography," *Opt. Lett.* **24**, 1221-1223 (1999).
 4. I. Hartl, X. D. Li, C. Chudoba, R. K. Hganta, T. H. Ko, J. G. Fujimoto, J. K. Ranka, and R. S. Windeler, "Ultrahigh-resolution optical coherence tomography using continuum generation in an air-silica microstructure optical fiber," *Opt. Lett.* **26**, 608-610 (2001).
 5. B. Povazay, K. Bizheva, A. Unterhuber, B. Hermann, H. Sattmann, A. F. Fercher, W. Drexler, A. Apolonski, W. J. Wadsworth, J. C. Knight, P. S. J. Russell, M. Vetterlein, and E. Scherzer, "Submicrometer axial resolution optical coherence tomography," *Opt. Lett.* **27**, 1800-1802 (2002).
 6. Y. Wang, Y. Zhao, J. S. Nelson, Z. Chen, and R. S. Windeler, "Ultrahigh-resolution optical coherence tomography by broadband continuum generation from a photonic crystal fiber," *Opt. Lett.* **28**, 182-184 (2003).
 7. K. Bizheva, B. Povazay, B. Hermann, H. Sattmann, W. Drexler, M. Mei, R. Holzwarth, T. Hoelzenbein, V. Wachter, and H. Pehamherger, "Compact, broad-bandwidth fiber laser for sub-2- μm axial resolution optical coherence tomography in the 1300-nm wavelength region," *Opt. Lett.* **28**, 707-709 (2003).
-

8. S. Bourquin, A. D. Aguirre, I. Hartl, P. Hsiung, T. H. Ko, J. G. Fujimoto, T. A. Birks, W. J. Wadsworth, U. Bunting, and D. Kopf, "Ultrahigh resolution real time OCT imaging using a compact femtosecond Nd : Glass laser and nonlinear fiber," *Opt. Express* **11**, 3290-3297 (2003), <http://www.opticsexpress.org/abstract.cfm?URI=OPEX-11-24-3290>
9. E. A. Swanson, D. Huang, M. R. Hee, J. G. Fujimoto, C. P. Lin, and C. A. Puliafito, "High-speed optical coherence domain reflectometry," *Opt. Lett.* **17**, 151-153 (1992).
10. C. A. Puliafito, M. R. Hee, C. P. Lin, E. Reichel, J. S. Schuman, J. S. Duker, J. A. Izatt, E. A. Swanson, and J. G. Fujimoto, "Imaging of macular diseases with optical coherence tomography," *Ophthalmol.* **102**, 217-229 (1995).
11. M. R. Hee, J. A. Izatt, E. A. Swanson, D. Huang, J. S. Schuman, C. P. Lin, C. A. Puliafito, and J. G. Fujimoto, "Optical coherence tomography of the human retina," *Archiv. Ophthalmol.* **113**, 325-332 (1995).
12. W. Drexler, U. Morgner, R. K. Ghanta, F. X. Kärtner, J. S. Schuman, and J. G. Fujimoto, "Ultrahigh-resolution ophthalmic optical coherence tomography," *Nature medicine* **7**, 502-507 (2001).
13. W. Drexler, H. Sattmann, B. Hermann, T. H. Ko, M. Stur, A. Unterhuber, C. Scholda, O. Findl, M. Wirtitsch, J. G. Fujimoto, and A. F. Fercher, "Enhanced visualization of macular pathology with the use of ultrahigh-resolution optical coherence tomography," *Archiv. Ophthalmol.* **121**, 695-706 (2003).
14. A. F. Fercher, C. K. Hitzenberger, G. Kamp, and S. Y. Elzaiat, "Measurement of Intraocular Distances by Backscattering Spectral Interferometry," *Opt. Commun.* **117**, 43-48 (1995).
15. G. Hausler and M. W. Linduer, "Coherence radar and spectral radar-new tools for dermatological diagnosis," *J. Biomed. Opt.* **3**, 21-31 (1998).
16. M. Wojtkowski, R. Leitgeb, A. Kowalczyk, T. Bajraszewski, and A. F. Fercher, "In vivo human retinal imaging by Fourier domain optical coherence tomography," *J. Biomed. Opt.* **7**, 457-463 (2002).
17. R. Leitgeb, C. K. Hitzenberger, and A. F. Fercher, "Performance of fourier domain vs. time domain optical coherence tomography," *Opt. Express* **11**, 889-894 (2003), <http://www.opticsexpress.org/abstract.cfm?URI=OPEX-11-8-889>
18. J. F. de Boer, B. Cense, B. H. Park, M. C. Pierce, G. J. Tearney, and B. E. Bouma, "Improved signal-to-noise ratio in spectral-domain compared with time-domain optical coherence tomography," *Opt. Lett.* **28**, 2067-2069 (2003).
19. M. A. Choma, M. V. Sarunic, C. H. Yang, and J. A. Izatt, "Sensitivity advantage of swept source and Fourier domain optical coherence tomography," *Opt. Express* **11**, 2183-2189 (2003), <http://www.opticsexpress.org/abstract.cfm?URI=OPEX-11-18-2183>
20. M. Wojtkowski, T. Bajraszewski, P. Targowski, and A. Kowalczyk, "Real-time in vivo imaging by high-speed spectral optical coherence tomography," *Opt. Lett.* **28**, 1745-1747 (2003).
21. S. H. Yun, G. J. Tearney, J. F. de Boer, N. Iftimia, and B. E. Bouma, "High-speed optical frequency-domain imaging," *Opt. Express* **11**, 2953-2963 (2003).
22. N. Nassif, B. Cense, B. H. Park, S. H. Yun, T. C. Chen, B. E. Bouma, G. J. Tearney, and J. F. de Boer, "In vivo human retinal imaging by ultrahigh-speed spectral domain optical coherence tomography," *Opt. Express* **29**, 480-482 (2004), <http://www.opticsexpress.org/abstract.cfm?URI=OPEX-12-3-367>
23. L. M. Smith and C. C. Dobson, "Absolute Displacement Measurements Using Modulation of the Spectrum of White-Light in a Michelson Interferometer," *Appl. Opt.* **28**, 3339-3342 (1989).
24. S. R. Chinn, E. A. Swanson, and J. G. Fujimoto, "Optical coherence tomography using a frequency-tunable optical source," *Opt. Lett.* **22**, 340-342 (1997).
25. B. Golubovic, B. E. Bouma, G. J. Tearney, and J. G. Fujimoto, "Optical frequency-domain reflectometry using rapid wavelength tuning of a Cr⁴⁺/forsterite laser," *Opt. Lett.* **22**, 1704-1706 (1997).
26. S. H. Yun, C. Boudoux, G. J. Tearney, and B. E. Bouma, "High-speed wavelength-swept semiconductor laser with a polygon-scanner-based wavelength filter," *Opt. Lett.* **28**, 1981-1983 (2003).
27. M. Wojtkowski, T. Bajraszewski, I. Gorczynska, P. Targowski, A. Kowalczyk, W. Wasilewski, and C. Radzewicz, "Ophthalmic Imaging by Spectral Optical Coherence Tomography," *Am. J. Ophthalmol.* (accepted).
28. R. Leitgeb, M. Wojtkowski, A. Kowalczyk, C. K. Hitzenberger, M. Sticker, and A. F. Fercher, "Spectral measurement of absorption by spectroscopic frequency-domain optical coherence tomography," *Opt. Lett.* **25**, 820-822 (2000).
29. R. A. Leitgeb, L. Schmetterer, W. Drexler, A. F. Fercher, R. J. Zawadzki, and T. Bajraszewski, "Real-time assessment of retinal blood flow with ultrafast acquisition by color Doppler Fourier domain optical coherence tomography," *Opt. Express* **11**, 3116-3121 (2003), <http://www.opticsexpress.org/abstract.cfm?URI=OPEX-11-23-3116>
30. R. A. Leitgeb, L. Schmetterer, C. K. Hitzenberger, A. F. Fercher, F. Berisha, M. Wojtkowski, and T. Bajraszewski, "Real-time measurement of in vitro flow by Fourier-domain color Doppler optical coherence tomography," *Opt. Lett.* **29**, 171-173 (2004).
31. M. Wojtkowski, A. Kowalczyk, R. Leitgeb, and A. F. Fercher, "Full range complex spectral optical coherence tomography technique in eye imaging," *Opt. Lett.* **27**, 1415-1417 (2002).
32. R. A. Leitgeb, C. K. Hitzenberger, A. F. Fercher, and T. Bajraszewski, "Phase-shifting algorithm to achieve high-speed long-depth-range probing by frequency-domain optical coherence tomography," *Opt. Lett.* **28**, 2201-2203 (2003).
33. P. Targowski, M. Wojtkowski, A. Kowalczyk, T. Bajraszewski, M. Szkulmowski, and W. Gorczynska, "Complex spectral OCT in human eye imaging in vivo," *Opt. Commun.* **229**, 79-84 (2004).

34. B. Bouma, G. J. Tearney, S. A. Boppart, M. R. Hee, M. E. Brezinski, and J. G. Fujimoto, "High-resolution optical coherence tomographic imaging using a mode-locked Ti-Al₂O₃ laser source," *Opt. Lett.* **20**, 1486-1488 (1995).
35. C. K. Hitzenberger, A. Baumgartner, W. Drexler, and A. F. Fercher, "Dispersion effects in partial coherence interferometry: implications for intraocular ranging," *J. Biomed. Opt.* **4**, 144-151 (1999).
36. A. F. Fercher, C. K. Hitzenberger, M. Sticker, R. Zawadzki, B. Karamata, and T. Lasser, "Numerical dispersion compensation for partial coherence interferometry and optical coherence tomography," *Opt. Express* **9**, (2001), <http://www.opticsexpress.org/abstract.cfm?URI=OPEX-9-12-610>
37. J. F. de Boer, C. E. Saxon, and J. S. Nelson, "Stable carrier generation and phase-resolved digital data processing in optical coherence tomography," *Appl. Opt.* **40**, 5787-5790 (2001).
38. D. L. Marks, A. L. Oldenburg, J. J. Reynolds, and S. A. Boppart, "Autofocus algorithm for dispersion correction in optical coherence tomography," *Appl. Opt.* **42**, 3038-3046 (2003).
39. R. L. Fork, C. H. B. Cruz, P. C. Becker, and C. V. Shank, "Compression of Optical Pulses to 6 Femtoseconds by Using Cubic Phase Compensation," *Opt. Lett.* **12**, 483-485 (1987).
40. B. E. Lemoff and C. P. J. Barty, "Cubic-Phase-Free Dispersion Compensation in Solid-State Ultrashort-Pulse Lasers," *Opt. Lett.* **18**, 57-59 (1993).
41. D. X. Hammer, A. J. Welch, G. D. Noojin, R. J. Thomas, D. J. Stolarski, and B. A. Rockwell, "Spectrally resolved white-light interferometry for measurement of ocular dispersion," *J. Opt. Soc. Am. A. Opt. Image Sci. Vis.* **16**, 2092-2102 (1999).
42. J. W. Goodman, *Statistical Optics* (Wiley, New York, 2000), p. 550.
43. K. Naganuma, K. Mogi, and H. Yamada, "Group-Delay Measurement Using the Fourier-Transform of an Interferometric Cross-Correlation Generated by White-Light," *Opt. Lett.* **15**, 393-395 (1990).
44. U. Morgner, F. X. Kartner, S. H. Cho, Y. Chen, H. A. Haus, J. G. Fujimoto, E. P. Ippen, V. Scheuer, G. Angelow, and T. Tschudi, "Sub-two-cycle pulses from a Kerr-lens mode-locked Ti:sapphire laser," *Opt. Lett.* **24**, 411-413 (1999).

1. Introduction

Optical coherence tomography is an emerging imaging technology that enables high-resolution, cross-sectional imaging in biological tissues and materials [1,2]. The development of ultrahigh-resolution optical coherence tomography using broadband light sources has enabled axial resolutions to approach the few micron scale [3-8]. Although ultrahigh resolution greatly improves image quality, if standard time domain detection techniques are used, there is a reduction in signal to noise with increasing detection bandwidth. Therefore, ultrahigh-resolution imaging requires a reduction in imaging speed [9].

Optical coherence tomography has been especially powerful for ophthalmic imaging, where it can provide images of retinal pathology with unprecedented resolutions [10,11]. The application of ultrahigh-resolution OCT in ophthalmic imaging has yielded axial resolutions of 3 μm in the retina; compared to 10 μm for standard resolution OCT [12,13]. Ultrahigh resolution greatly improves the ability to differentiate architectural morphology in the retina and visualize subtle changes associated with early disease. However, since light exposure levels in the eye are limited for safety reasons, the imaging speeds for ultrahigh-resolution OCT achieved by standard time domain detection techniques are very limited.

Fourier domain optical coherence tomography (FdOCT) [14,15] offers significantly improved sensitivity and imaging speed when compared to time domain OCT [16-22]. In Fourier domain OCT, the magnitude and delay of backscattered or backreflected light is measured by spectral analysis of the interference pattern. Fourier domain OCT detection can be performed in two ways; spectral domain OCT (spectral OCT) using a spectrometer with a multichannel analyzer [14,15,23], or swept source OCT using a rapidly tunable laser source [19,21,24-26]. Spectral domain OCT at standard resolution has been applied to ophthalmic imaging in the anterior eye and retina and has demonstrated superior imaging speeds when compared to time domain OCT [16,20,22]. Spectral domain and swept source OCT are especially promising for ultrahigh-resolution imaging because they overcome imaging speed limitations of time domain OCT. Therefore, it is possible to use these techniques to form three-dimensional maps of the macula and optic disk [22,27]. This enables cross-registration of three-dimensional data sets with fundus photographs for a more accurate diagnosis of disease and evaluation of treatment. In addition, Fourier domain OCT has the advantage of providing direct access to the spectral fringe pattern, thus enabling a wide range of novel applications. Spectral domain OCT can be used for absorption measurement [28], Doppler

techniques can be used to image blood flow [29,30], and the complex Fourier domain signal can be directly measured to double the axial measurement range [31-33].

Ultrahigh-resolution OCT imaging requires light of broad spectral bandwidth, therefore dispersion compensation is important in order to achieve ultrahigh resolution. In time domain OCT with analog demodulation, dispersion compensation is usually performed by matching the optical materials and path lengths in the two interferometer arms [3,12,34,35]. Grating-based phase delay scanners can also be used to provide dispersion compensation concurrently with group and phase delay scanning [25]. These methods work well if the dispersion in the sample arm is fixed, but they require readjustment if the dispersion varies between samples. In time domain OCT with digital fringe detection, dispersion can be compensated by using numerical techniques. Several techniques have been demonstrated including convolution with a depth-dependent kernel [36], correction of quadratic phase distortion using an isolated calibration reflection [37], and optimization of a functional with respect to the dispersion parameters [38].

In addition to enabling a dramatic increase in imaging speed, spectral domain and swept source OCT are particularly well suited for numerical dispersion compensation, because the spectral fringe signal is directly available during the signal processing required to generate the image. Numerical dispersion compensation is especially powerful for applications such as ultrahigh-resolution retinal imaging, because variations in eye length between different subjects can cause dispersion mismatch and, therefore, resolution loss.

In this manuscript, we describe ultrahigh-resolution, high-speed spectral domain OCT. Using a broadband laser light source, an axial resolution of $2.7 \mu\text{m}$ in air, corresponding to $2.1 \mu\text{m}$ in tissue, is achieved. To our knowledge, this is the highest axial resolution achieved in spectral domain OCT to date. Imaging speeds of 16,000 axial scans per second with 1024 pixels per axial scan are demonstrated. Ultrahigh-resolution high-speed OCT imaging is performed in the retina. A factor of $\sim 100x$ increase in imaging speed, when compared to time domain OCT, is shown. We describe techniques for numerical dispersion compensation that achieve comparable or better performance than standard dispersion matching techniques. An automatic iterative optimization method for dispersion compensation in ultrahigh-resolution OCT images is also presented. These techniques are general and can be applied to spectral domain as well as swept source OCT. Factors that influence ultrahigh-resolution OCT system design and performance are also discussed.

2. Theory

In spectral domain OCT, cross-sectional images are generated by measuring the echo time delay and magnitude of backreflected or backscattered light in the Fourier domain. The sample is illuminated with broadband light. Backreflected or backscattered light signals from different depths that correspond to different delays are brought to interference with light from a reference path with a known delay. The interference produces fringes, which are detected by a spectrometer using a high-speed multi-element CCD or photodiode array detector. The delay and magnitude of the optical reflections from the sample can be detected by Fourier transforming the spectral interference signal. It is important to note that the phase of the interference fringe pattern will shift if the sample distance changes by a significant fraction of a wavelength in the axial direction. Therefore, exposure times must be short in order to avoid fringe averaging and loss of signal if there is motion of the sample.

Spectrometers measure optical intensity as a function of wavelength. In order to apply the discrete Fourier transform (DFT) reconstructing the axial scan as a function of τ (or z), the spectrum should be evenly sampled in the conjugate variable ω (or k). Therefore, the spectrometer output must be converted from wavelength λ to frequency ω using a hyperbolic scale transformation. The detected spectrum, as a function of frequency, is given by:

$$S_{out}(\omega) = |E_R(\omega)|^2 + 2 \operatorname{Re}\{E_R(\omega)^* E_S(\omega)\} + |E_S(\omega)|^2 \quad (1)$$

where E_R is the reference arm field and E_S is the field from the sample, including delays and attenuation. The intensity from the sample arm is usually small compared to the intensity from the reference arm, so the last term in Eq. (1) can be ignored. Additionally, subtracting the spectrum of the reference light, provides the pure interferometric signal $S_{int}(\omega)$, which carries the useful information. It is a sum of fringes that are generated by the interference of light reflected from different interfaces within an object with the light reflected from the reference mirror:

$$S_{int}(\omega) = 2 \operatorname{Re}\{E_R(\omega)*E_S(\omega)\} = 2 \operatorname{Re}\left\{\sum_n \sqrt{I_n(\omega)I_r(\omega)} \exp[i(\omega\tau_n + \Phi(\omega, \tau_n))]\right\}. \quad (2)$$

Here I_n is the intensity of light reflected from the n-th layer in the sample, I_r is the intensity of light reflected from the reference arm, and τ_n is the optical group delay of the n-th reflection, relative to the reference light path. $\Phi(\omega, \tau_n)$ is a general frequency and delay-dependent phase that includes higher order dispersive terms. The axial measurement of backscatter or backreflection, also known as an axial scan, is obtained by taking the Fourier transform of Eq. (2).

2.1 Axial image resolution in ultrahigh-resolution spectral domain OCT

In OCT, the axial image resolution Δz is inversely proportional to the bandwidth of the light source used for imaging:

$$\Delta z = \frac{2 \ln 2}{\pi} \frac{\lambda_0^2}{\Delta \lambda}, \quad (3)$$

where $\Delta \lambda$ is the full width half maximum (FWHM) of the light source and λ_0 is the center wavelength.

In spectral domain OCT, the CCD or array detector in the spectrometer has a limited bandwidth or spectral range, $\Delta \Lambda$. If $\Delta \Lambda$ is too small and the full available spectrum is not imaged onto the CCD, the axial resolution will be inferior to the theoretical value set by Eq. 3. In other words, the axial pixel spacing, which is defined by the spectral range $\Delta \Lambda$, must be small enough to support the axial resolution. If $\Delta \Lambda$ is too large, the pixel spacing and the axial measurement range are reduced without improving the axial resolution. Therefore, $\Delta \Lambda$ must be chosen so that the optimal resolution in Eq. (3) is achieved without compromising the axial measurement range. Choosing a pixel spacing of $\Delta z/2$ that corresponds to one-half the theoretical axial resolution Δz enables two reflections separated by Δz to be resolved. Thus, the spectrometer must have a bandwidth or spectral range of [16]:

$$\Delta \Lambda = \frac{1}{2} \frac{\lambda_0^2}{\Delta z/2} = \frac{\pi}{2 \ln 2} \Delta \lambda. \quad (4)$$

If the spectrometer has a bandwidth or spectral range given by the above equation and the detector has N pixels, then the axial measurement range ΔL_z over which reflected signals can be measured is given by:

$$\Delta L_z = \frac{\Delta z}{2} \frac{N}{2} = \frac{\ln 2}{2\pi} \frac{\lambda_0^2}{\Delta \lambda} N \quad (5)$$

The total number of pixels carrying unique information about the axial scan is reduced by a factor of two, because the Fourier transform of the real spectrum has conjugate symmetry about the zero delay [31]. The above equation shows that, for a given source bandwidth, the axial scan range is determined by the number of pixels, if optimal resolution (given by Eq. (3)) is to be achieved.

In spectral domain OCT, the sensitivity varies across the axial measurement range due to the finite spectral resolution of the spectrometer. The finite spectral resolution is caused by the finite spot size and by the finite detector element size. Both cause integration over a range of wavelengths for one pixel; therefore, there is a loss in fringe visibility for larger axial delays [17,22].

2.2 Dispersion compensation in ultrahigh-resolution spectral domain OCT

Ultrahigh-resolution OCT requires extremely broad spectral bandwidths. In order to achieve the optimal resolution consistent with the light source bandwidth, it is necessary to carefully match dispersion between the two arms of the interferometer. Dispersion arises because of frequency dependence in the propagation constants $\beta(\omega)$ for materials in the interferometer arms or the sample. In ultrafast lasers and in ultrafast measurement, compensation of dispersion is essential in order to preserve pulse durations and to achieve high time measurement resolutions [39,40]. In ultrahigh-resolution OCT, only the dispersion mismatch between the reference and sample arms must be compensated for optimal resolution. For any given material, the propagation constant $\beta(\omega)$ can be expanded as a Taylor series near the center frequency of the light source ω_0 , as shown below:

$$\beta(\omega) = \beta(\omega_0) + \left. \frac{d\beta}{d\omega} \right|_{\omega_0} (\omega - \omega_0) + \frac{1}{2} \left. \frac{d^2\beta}{d\omega^2} \right|_{\omega_0} (\omega - \omega_0)^2 + \frac{1}{6} \left. \frac{d^3\beta}{d\omega^3} \right|_{\omega_0} (\omega - \omega_0)^3 + \dots \quad (6)$$

The constant term $\beta(\omega_0)$ is the propagation constant at the center wavelength ω_0 of the spectral bandwidth, while the second term $d\beta(\omega)/d\omega$ is the inverse group velocity. The third term $1/2d\beta^2(\omega)/d\omega^2$ describes the group velocity dispersion or a variation in group velocity with frequency. This is the term that produces pulse broadening in femtosecond optics and broadening of the axial resolution in OCT. The fourth term $1/6[d\beta^3(\omega)/d\omega^3](\omega - \omega_0)^3$ has been referred to as third-order dispersion, which produces asymmetric pulse distortion in femtosecond optics and asymmetric distortion of the point spread function in OCT. Higher order terms may also be present.

In OCT, achieving ultrahigh-axial image resolution requires that the dispersion in the two arms of the interferometer be matched over the bandwidth of the light source. In OCT using time domain detection, the dispersions in the interferometer sample and reference arms must be carefully matched by using identical lengths of identical optical materials in both arms [3,12]. This ensures that all orders of the dispersion are matched. If the light wave in the signal path of the interferometer propagates through a length of dispersive material that is not matched by a similar material in the reference path, a frequency- and delay-dependent phase shift $\Phi(\omega, \tau_n)$ is imparted to the signal. In spectral domain OCT, this phase shift appears in the expression for the spectral fringe pattern, Eq. (2). Since the axial scan measurement of backreflection or backscattering, versus delay or distance, is performed by determining the Fourier transformation of the spectral fringes, multiplying the spectrum by a nonlinear phase prior to Fourier transforming will result in a loss of axial resolution.

In most OCT imaging applications, the axial range ΔL_z over which imaging is performed is short. In scattering tissues, the imaging depth is limited by optical scattering and absorption. For ultrahigh-resolution spectral domain OCT, the axial range ΔL_z is further limited by the number of pixels. Therefore, variation of dispersion over the axial image range is usually negligible, and dispersion is predominantly caused by fixed material in front of the axial imaging range. Because the frequency-dependent phase distortion is the same for all depths in one axial scan, the dispersion is not depth dependent. In this case, the phase shift $\Phi(\omega, \tau_n)$ becomes independent of delay or axial position $\Phi(\omega, \tau_n) = \Phi(\omega)$. In retinal imaging, the beam propagates through the cornea, aqueous, lens, and vitreous of the eye before it reaches the retina. The majority of ocular dispersion occurs from propagation through the vitreous, which comprises the majority of the eye length [41]. Different subjects have different eye lengths, so dispersion compensation may need to be adjusted for individual

subjects. The axial scanning range ΔL_z is usually on the order of 1-2 mm, so the dispersion is, to a good approximation, depth independent over this range.

In spectral OCT, dispersion compensation can be performed by canceling the frequency-dependent nonlinear phase in Eq. (2), which arises from the dispersion mismatch between the two arms of the interferometer. Figure 1 shows a flowchart schematic of the signal processing used in spectral OCT. First, in order to eliminate the reference power term (Eq. (1)), a reference spectrum from only the reference arm is detected and subtracted from the interference spectrum. This reference spectrum is acquired at the beginning of every image acquisition in order to account for fluctuations in the source between measurements. The resultant interference signal $S_{int}(\omega)$ is rescaled to convert from wavelength to frequency and is resampled. This rescaling corrects for the hyperbolic $\omega \sim 1/\lambda$ dependence of the spectrum on wavelength. Any other corrections for spectrometer calibration can also be implemented by generalizing the rescaling function. Since the spectral fringe pattern from the spectrometer is a real function, a Hilbert transform is used to generate the imaginary part of the complex analytic signal of the spectral fringe pattern $\text{Im}\{\hat{S}(\omega)\}$ [42]. Note that this is not equivalent to acquiring the complex interference signal directly, since the number of pixels carrying unique information about the axial measurement is reduced by a factor of two from the number of pixels in the spectrum [31]. The real and imaginary parts of the spectral fringe pattern are used to construct the complex analytic representation of the spectral fringe pattern $\hat{S}(\omega) = |S(\omega)|\exp(i\phi(\omega))$. The phase of $\hat{S}(\omega)$ is then modified by adding a phase correction to compensate dispersion:

$$\bar{\Phi}(\omega) = -a_2(\omega - \omega_0)^2 - a_3(\omega - \omega_0)^3 \quad (7)$$

The coefficient $-a_2$ is adjusted to cancel the group velocity dispersion imbalance (second-order term) and $-a_3$ is adjusted to cancel the third-order dispersion imbalance (third-order term). This method may be generalized to higher orders; however, compensation to third-order is usually sufficient, assuming that the interferometer arms were approximately dispersion matched initially. Finally, the corrected spectrum is Fourier transformed to obtain the axial depth scan. If the appropriate phase correction has been applied, this new axial depth scan is compensated for dispersion mismatch between the interferometer arms and has optimum axial resolution.

2.3 Automatic dispersion compensation in ultrahigh resolution Spectral domain OCT

In general, the dispersion mismatch with a sample in the interferometer is not known, so the coefficients in the phase compensation equation, Eq. (7), must be determined. If an isolated specular reflection is available, the phase of the spectral fringe signal can be determined by using the Fourier transform of the interference spectrum. This method is similar to that used in femtosecond optics for measuring dispersion in materials [43]. However, this method cannot be used in most OCT images because isolated reflections are often not available. OCT images are usually composed of multiple backreflecting and backscattering features. Thus, the phase of the spectral fringes is complicated and does not represent the phase dependence from the dispersion mismatch alone.

Nevertheless, dispersion may be automatically compensated in OCT images using an iterative procedure that measures and optimizes the sharpness of the image. This procedure is shown schematically in Fig. 1. In order to determine the optimal phase correction function automatically, we use a sharpness metric function, $M(a_2, a_3)$, which is maximized when the image is sharpest. Many possible functions can be used, however, for this study, we defined $M(a_2, a_3)$ to be one divided by the total number of points in the axial scan intensity (the power spectrum of the interferometric fringe pattern) which are above a predetermined threshold.

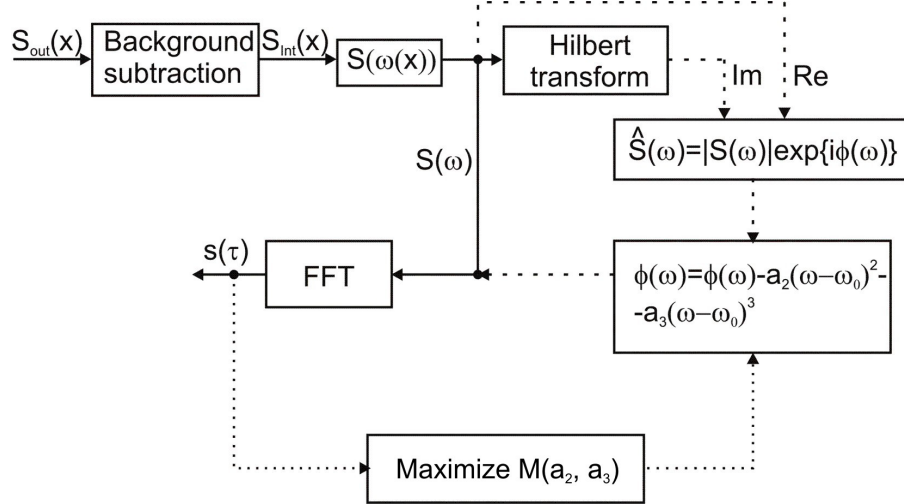


Fig. 1. Flow chart of spectral OCT dispersion compensation procedure. The interference spectrum is first rescaled to convert from wavelength to frequency and then resampled. In standard spectral OCT, this spectrum is Fourier transformed to calculate the axial scan, which gives backreflection/backscattering versus distance (solid path). For dispersion compensation (dashed path), the Hilbert transform is used to calculate the complex representation of the input signal. The phase of this signal is modified by using adjustable second- and third-order terms. The modified spectrum is Fourier transformed to calculate the axial scan. In order to perform automatic dispersion compensation, the sharpness of the axial scan or image is measured. The second- and third-order phase correction is iteratively adjusted to achieve optimum sharpness, as shown in the dotted path. This procedure may be generalized to correct higher orders of dispersion.

The function $M(a_2, a_3)$ essentially measures the concentration of energy in the image. By Parseval's theorem, the dispersion correction procedure does not change the total energy. $M(a_2, a_3)$, is maximized by varying the second- and third-order coefficients a_2 and a_3 , which correspond to adjusting the group velocity dispersion and third-order dispersion. The coefficients can usually be optimized independently, proceeding from lower to higher order, since the third-order dispersion mismatch is usually small. This procedure can also be generalized to higher order dispersion compensation at the expense of increasing complexity. This method is particularly well suited for OCT images that have thin, sharp features such as retinal images, since the thin structures produce sharp features with a small number of points when the function is maximized. However, this method will work in almost any OCT image with adequate contrast.

3. Methods

A schematic of the ultrahigh-resolution spectral domain OCT system is shown in Fig. 2. The laser light source is a broadband, femtosecond KLM Ti:Sapphire laser using double-chirped mirrors [44]. In this study, a bandwidth of $\Delta\lambda = 144$ nm FWHM centered at 850 nm is used. A broadband fiber optic splitter and broadband components are used in the interferometer. In order to perform ophthalmic imaging of the retina, the sample arm is interfaced to a slitlamp biomicroscope that relay images and scans the OCT beam on the retina [11,12]. The reference arm of the interferometer has an adjustable delay reflector and dispersion is initially matched between the sample and reference arms by using different lengths of optical materials. The output of the interferometer is analyzed by a spectrometer. The spectrometer consists of an IR achromat doublet $f = 45$ mm fiber collimating lens, a 1200 line/mm volume phase holographic grating with 80% efficiency, and an $f = 75$ mm lens (composed of two air spaced IR achromat doublet $f = 150$ mm lenses) that images the spectrum onto a 2048 element CCD linescan camera. The optical efficiency of the spectrometer defined as the power incident on the CCD divided by the power in the fiber is approximately 78%. The camera has

a 12-bit resolution with a maximum data transfer rate of 60 MHz. Data is digitized and transferred to computer (Pentium IV, 3.2 GHz, 1 GB RAM) system memory by a frame grabber.

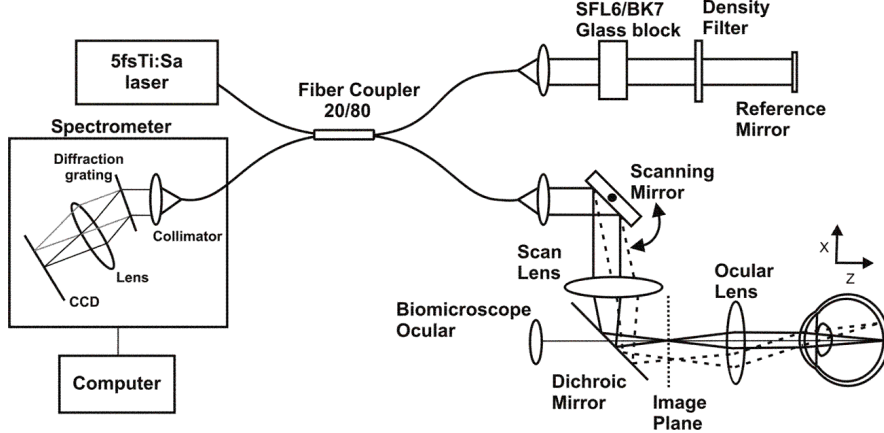


Fig. 2. Schematic diagram of the ultrahigh-resolution spectral domain OCT system. Retinal imaging is performed by using a modified slitlamp biomicroscope. Optical materials are used in the reference arm to compensate for dispersion mismatch between the reference and sample arm optical components. The spectrometer consists of a collimating lens, a transmission grating, and a lens that images the spectrum onto a 2048-element CCD linescan camera.

The spectrometer bandwidth range $\Delta\Lambda$ was designed to match the bandwidth of the light source, as described in Eq. (4). The spectrometer was calibrated at five wavelengths across its bandwidth by comparing the spectrum registered by the CCD with a commercial optical spectrum analyzer. The bandwidth of the OCT spectrometer was $\Delta\Lambda = 266$ nm (Fig. 3), which corresponds to a spectral resolution $\delta\lambda$ of 0.13 nm / pixel for 2048 pixels.

Two modes of operation, a real-time display mode and an acquisition mode are possible. In the real-time display mode, OCT images are acquired, processed, and displayed at a rate of 7 frames per second (1024 x 512 pixels/frame) to facilitate alignment. In the acquisition mode, data is acquired at 31 frames per second (1024 x 512 pixels/frame). Images with higher transverse pixel density could also be acquired at lower frame rates. After acquisition, image reconstruction is performed by subtracting the reference spectrum, rescaling the inference spectrum from wavelength to frequency ($\omega = 2\pi c/\lambda$) by using spline interpolation and resampling, followed by dispersion compensation and Fourier transformation.

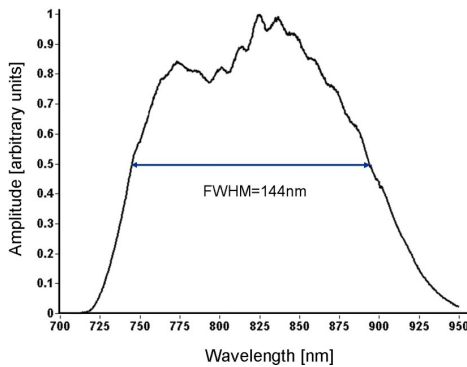


Fig. 3. Spectrum from the Ti:Sapphire laser source registered by the OCT spectrometer, as shown in Fig. 2. The bandwidth is 144 nm FWHM.

4. Results

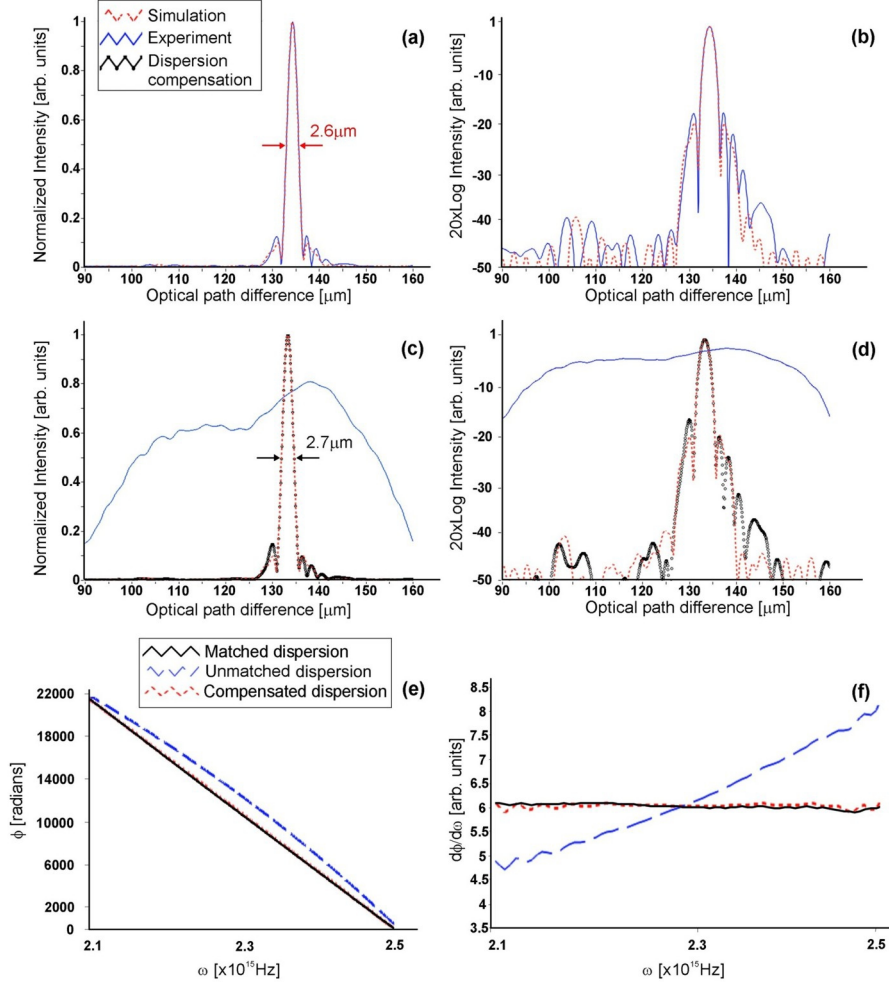


Fig. 4. Characterization of point spread function with matched (no water cell in reference arm) and unmatched (2 cm water cell in reference arm) dispersion. a, b) Comparison of theoretically calculated and experimentally measured point spread functions (PSF) with dispersion matched between the reference and sample arms. c, d) Comparison of the theoretical PSF, measured PSF with unmatched dispersion, and measured PSF with unmatched dispersion and numerical compensation. e) Phase comparison of the measured PSF with matched dispersion, the measured PSF with unmatched dispersion, and the measured PSF with unmatched dispersion and numerical dispersion correction. f) Comparison of the phase derivative (proportional to inverse of group velocity) for the same three cases. In all cases, dispersion is compensated by iteratively adjusting second- and third-order terms to maximize the sharpness metric M.

Using the laser light source, the measured FWHM of the spectrum is $\Delta\lambda = 144$ nm, which corresponds to a theoretically predicted axial resolution of $\Delta z \sim 2.1$ μm in air. However, because the shape of the spectrum is not perfectly Gaussian, the effective axial resolution is less than this optimum value. In order to find the theoretical value of the axial resolution, the square roots of the individual spectra from the reference and sample arms are multiplied and modulated digitally. Fourier transformation of this signal yields the theoretically calculated point spread function with a FWHM of $\Delta z \sim 2.1$ μm in air, as shown in Fig. 4(a). The experimentally measured point spread function has a FWHM of $\Delta z = 2.7$ μm in air. The

corresponding axial resolution in tissue is $\sim 2.1 \mu\text{m}$. The axial pixel size is measured to be $1.35 \mu\text{m}$, corresponding to an axial measurement range of $\Delta L_z = 1.38 \text{ mm}$. This design makes full use of the optical bandwidth, while maximizing the scanning range ΔL_z .

The dispersion in the two arms of the interferometer was balanced and the point spread function experimentally measured. In order to increase the digital resolution to $0.1 \mu\text{m}$ in the FWHM measurement, the spectral data is zero-padded to 2^{15} pixels before Fourier transformation. The point spread function is shown for an optical path difference of $135 \mu\text{m}$, and is not centered at zero because, in spectral OCT, the FWHM and the sensitivity depend on position.

The FWHM of the point spread function at different axial delays is plotted in Fig. 5. The axial resolution in air varies between $2.7 \mu\text{m}$ near zero delay and $3.7 \mu\text{m}$ at the edge of the axial measurement range. The spectrometer has limited resolution and furthermore, because the spectrometer uses lenses, the resolution varies as a function of wavelength, with the optimum resolution at the center wavelength and decreasing resolution at the edges of the spectrometer bandwidth range. Since different delays are mapped into different frequencies of spectral interference fringes (Eq. (2)), the axial resolution can depend upon delay or axial position. Figure 5(b) shows a comparison between spectral fringe patterns for reflections near zero delay and at the edge of the measurement range. The broader interference pattern observed for smaller delays yields a narrower point spread function. The loss in fringe visibility at the edge of the spectrometer may be caused by curvature in the focal plane of the spectrometer and aberrations in the spectrometer lenses. These measurements are performed at a speed of one axial scan of 2048 elements per $62 \mu\text{s}$, or a data rate of 33 MHz . The exposure time for one axial scan is $50 \mu\text{s}$. The maximum sensitivity is 98 dB for $750 \mu\text{W}$ of incident optical power. The dynamic range is 71 dB . Sensitivity is measured at different delays and is plotted in Fig. 5(c). There is a drop in sensitivity of 18 dB over the 1.4 mm delay measurement range. This degradation is caused by the resolution limit of the spectrometer from the focused spot size on the CCD, the finite pixel width, and resolution limiting aberrations. These effects cause a reduction in fringe visibility. Resolution-limiting effects can be modeled as a convolution in the spectral domain, which in the spatial domain corresponds to multiplying the axial delay scan by two envelopes; one corresponding to the finite pixel size and the other corresponding to the finite spot size [16,22].

4.1 Dispersion compensation

To demonstrate numerical dispersion compensation, the dispersion in the sample and reference arms of the interferometer is deliberately mismatched by placing a 2-cm-length water cell in the sample arm. This 2-cm-length water cell has dispersion similar to that of the human eye [41]. The axial resolution FWHM of the point spread function using numerically compensated dispersion is also measured as a function of delay and is shown in Fig. 5(a). The axial resolution obtained by numerical dispersion compensation is in good agreement with that measured with physically matched dispersion. In some cases, numerically compensated dispersion can yield a better resolution than physically matched dispersion, because numerical compensation provides a more sensitive adjustment than is possible experimentally.

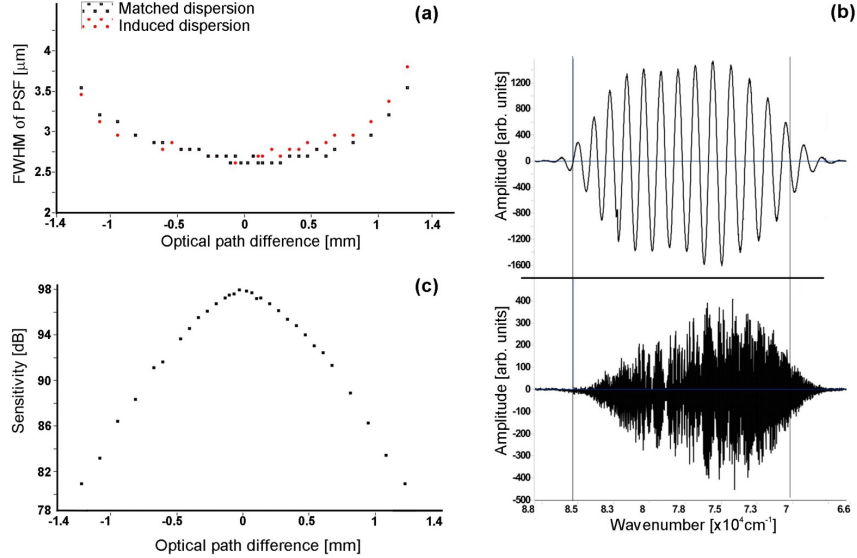


Fig. 5. a) Plot of axial resolution (FWHM of the measured point spread function) with matched dispersion and unmatched dispersion with numerical compensation. Dispersion is induced with a 2 cm water cell in the reference arm. The FWHM increases with optical path difference due to the loss of fringe visibility away from the center wavelength of the spectrometer λ_0 . The loss in fringe visibility is more severe for larger optical path differences. This effect is shown in b), where the interferometric fringes after the scale transformation are shown for sample reflections from 0.05 mm (top) and 1.2 mm (bottom). c) The maximum sensitivity is achieved for zero optical path difference and it decreases by 18 dB over the 1.4 mm scan range.

4.2 Ultrahigh-resolution retinal imaging

Ultrahigh-resolution ophthalmic OCT imaging was performed in normal human subjects. Investigations followed human subject protocols approved by the Institutional Review Board at the Tufts-New England Medical Center and the Committee on the Use of Humans Subjects at the Massachusetts Institute of Technology. Figure 6(a) shows an example of an OCT image of the macula with a 2.5 cm water cell inserted in the reference arm of the interferometer to match the dispersion in the eye. The spectral domain OCT image contains 3000 axial scans acquired at 16,000 axial scans per second or 150 milliseconds per image. In order to demonstrate the optimum ultrahigh-resolution imaging performance, high transverse pixel density images were obtained. These high density images could be pixel averaged (to yield lower density images consistent with computer screen display) to improve smoothness or zoomed to examine small features. Figure 7 shows that even in the 4x zoomed image, image quality is excellent and intraretinal layers are clearly demarcated. The ultrahigh-resolution images enable excellent visualization of the architectural morphology of the internal retinal layers. The nerve fiber layer (NFL), the ganglion cell layer (GCL), the inner plexiform layer (IPL), the inner nuclear layer (INL), the outer plexiform layer (OPL), the outer nuclear layer (ONL), the external limiting membrane (ELM), the photoreceptor inner and outer segment junction (IS/OS), the retinal pigment epithelium (RPE), and the choriocapillaris (CC) are visible in the ultrahigh-resolution image.

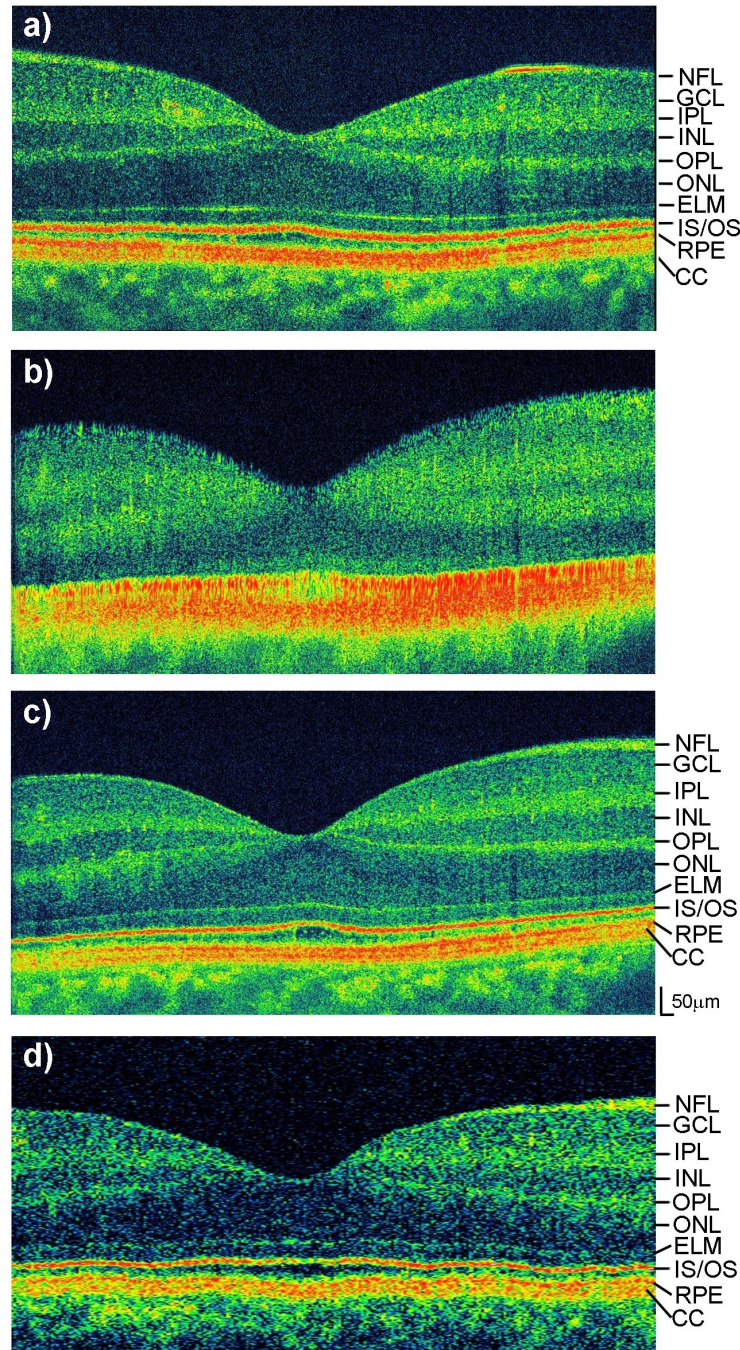


Fig. 6. a) Ultrahigh-resolution spectral OCT image of human macula with dispersion matched by a water cell in the reference arm. b) Image with unmatched dispersion. c) Same image with dispersion numerically corrected to second and third orders. The image with numerically compensated dispersion has a resolution comparable to or better than the image with physically matched dispersion. These spectral OCT images consist of 3000 axial scans acquired in 150 ms. d) Ultrahigh-resolution OCT image obtained by using time domain detection. The image consists of 300 axial scans acquired in 2 seconds.

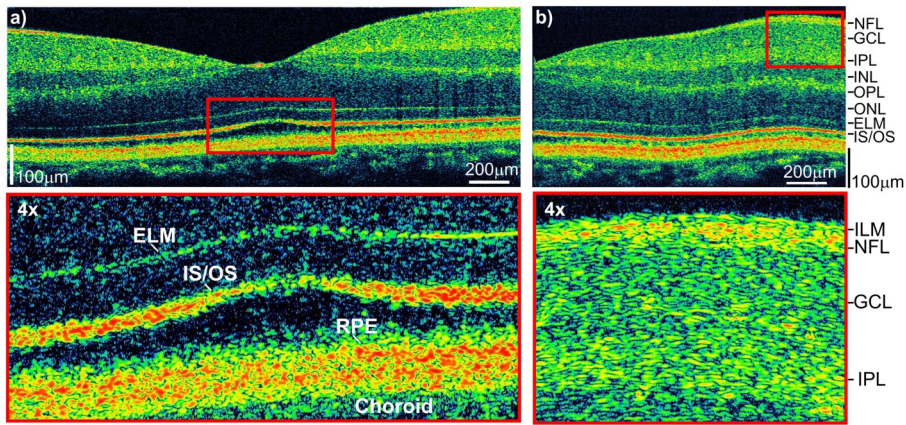


Fig. 7. Spectral OCT images of the human retina *in vivo*. Scans were taken along the papillomacular axis with 3000 axial scans acquired in 150 ms. a) The high transverse pixel density and high sensitivity allow a better discrimination of thin retinal layers, including the external limiting membrane (ELM), the photoreceptor inner and outer segment junction (IS/OS), and the retinal pigment epithelium (RPE). b) The inner limiting membrane (ILM) can also be discriminated from the nerve fiber layer (NFL) in the 4x image. Note that the image quality is maintained in the zoomed images due to the high transverse pixel density.

Dispersion compensation was investigated and demonstrated in retinal imaging. Figure 6(a) shows an OCT macular image acquired with a water cell in the reference arm to compensate ocular dispersion. Figure 6(b) shows an OCT macular image acquired with mismatched dispersion, where the reference arm of the interferometer did not contain a water cell to compensate ocular dispersion. The broad bandwidths used in ultrahigh-resolution OCT result in a severe degradation in image resolution for this large dispersion mismatch. Figure 6(c) shows the same OCT macular image, where the mismatched dispersion was numerically compensated. A dramatic improvement in resolution is evident and all retinal layers are well differentiated. A comparison of the image with numerically compensated dispersion, Fig. 6(c), to the image with physically matched dispersion, Fig. 6(a), shows that numerical dispersion compensation can yield better image sharpness than physically matched dispersion, because numerical compensation can provide a more sensitive adjustment than is possible experimentally.

Figure 6(d) shows a comparison with an ultrahigh-resolution OCT image acquired by using time domain detection with a scanning reference delay. This image has 300 axial scans acquired at a rate of 150 axial scans per second, or 2 seconds per image. Spectral domain OCT acquires images at 16,000 axial scans per second, compared to time domain OCT which acquires images at 150 axial scans per second. Thus, spectral domain OCT provides a ~100x increase in axial scan rates when compared to time domain OCT.

Although the axial image resolutions are comparable in the spectral domain and the time domain OCT images, the increase in the transverse pixel density which is possible using spectral domain OCT significantly improves the visualization of retinal architecture. The low-backscattering ganglion cell layer (GCL) and the thin, low-backscattering external limiting membrane (ELM) are better resolved. The increased pixel density of the spectral domain image also enhances the delineation of the boundaries between transparent and highly scattering layers such as the nerve fiber layer (NFL), the inner plexiform layer (IPL), the outer plexiform layer (OPL), the photoreceptor inner and outer segment junction (IS/OS), and the retinal pigment epithelium (RPE). In addition, intraretinal interfaces such as the external limiting membrane, the photoreceptor inner and outer segment junction, and the retinal pigment epithelium, which appear to be discontinuous in the low transverse pixel density,

time domain ultrahigh-resolution OCT image, appear to be continuous in the higher transverse pixel density, spectral domain ultrahigh-resolution OCT image. This improvement in image quality in high transverse pixel density images should significantly improve the performance of automated segmentation algorithms for measuring retinal architecture in three-dimensional data sets.

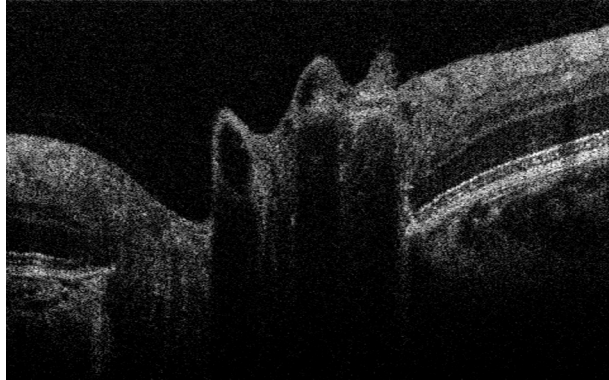


Fig. 8. (2.8 MB) High-speed spectral OCT movie of the optic disk using numerical dispersion compensation. This movie was acquired using images with 512 axial scans of 1024 pixels at a rate of 31 frames per second.

Figure 8 is an example of ultrahigh-speed, ultrahigh-resolution imaging of the optic disk at 31 frames per second with images of 512 transverse and 1024 axial pixels. These images were acquired with unmatched dispersion and were post processed to numerically compensate dispersion to second and third order. Note the sharpness of the image and the uniformity of the sharpness over the depth range. The retinal layers and the RPE terminate at the margin of the optic disc. Blood flow is seen as a fluctuating speckle pattern and pulsating motion of the retinal blood vessels that converge near the rim of the optic disc.

4.3 Automatic dispersion compensation in ultrahigh-resolution images

The image in Fig. 6(c) was obtained by optimizing the dispersion compensation parameters using the previously described automated method. The speed of the automatic optimization of the dispersion coefficients depends on the degree of unbalanced dispersion that is introduced. For the case that is demonstrated in the paper, the dispersion unbalance is caused by the beam propagation through the cornea, aqueous, lens, and vitreous of the eye. In the experiment, which results are shown in Fig. 6(c) and Fig. 9 the automatic optimization of parameters a_1 and a_2 took approximately 15 seconds. Once the optimized coefficients were determined, the dispersion correction was performed at 5 frames per second with a Pentium IV 3.2 GHz processor. Please note that it is necessary to calculate the optimization parameters a_1 and a_2 only once for each sample. In order to illustrate dispersion compensation procedure, Fig. 9 shows plots of the image sharpness metric function M as a function of coefficients a_2 and a_3 , which correspond to varying second- and third-order dispersion compensation. In this experiment, the optimum value of a_2 for second-order dispersion compensation is found iteratively, followed by third-order dispersion compensation. Both plots show well-defined optimization of the image sharpness metric function. The optimized values of a_2 and a_3 agree with those determined by visual adjustment of image sharpness by the operator. In addition, the optimum value of second-order dispersion compensation $a_2 = 497 \text{ fs}^2$ agrees well with the expected second-order dispersion of the eye, which is calculated from the dispersion of water, assuming a standard eye length of 24 mm. Dispersion is not physically matched in these experiments in order to demonstrate the performance of the numerical approach. However, for most imaging applications, dispersion in the sample and reference arms will be nearly matched. Therefore, only second-order dispersion compensation is required, except in cases

where the wavelength of operation has almost zero group velocity dispersion (e.g., near 1300 nm).

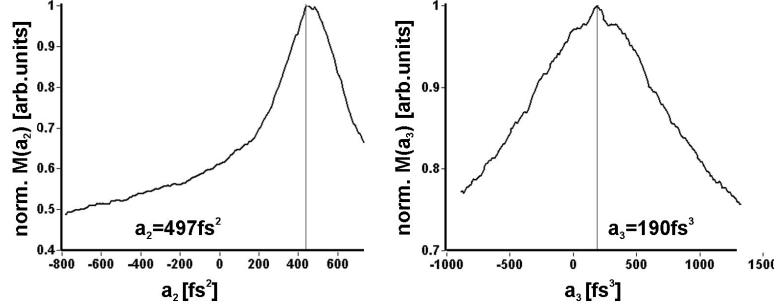


Fig. 9. The sharpness metric M defined in the theory section is shown for both second- and third-order dispersion correction, as applied to 300 A-scans in Fig. 6(b). The metric was first optimized with respect to a_2 and then with respect to a_3 . Each curve has a well-defined maximum, which corresponds visually to the sharpest image. The dispersion-corrected image is shown in Fig. 6(c).

4.4 Method for high-speed, approximate dispersion compensation

Numerical dispersion compensation is more computationally intensive than standard Fourier domain signal processing. However, it is possible to perform approximate dispersion compensation with no increase in computational time compared to standard spectral domain OCT. High-speed dispersion compensation can be performed by changing the hyperbolic scale transformation function applied to the spectral fringe data. The hyperbolic scale transformation $\omega \sim 1/\lambda$ between wavelength and frequency requires choosing a scale parameter which sets the bandwidth of the mapping of wavelength to frequency. A larger scale parameter increases the nonlinearity of this transformation. In order to correct for the sampling nonlinearity, the scale parameter of the scale transformation function should be set so the bandwidth is equal to $\Delta\Lambda$, the spectrometer bandwidth or spectral range. A different scale parameter in this scale transformation causes a position-dependent nonlinearity in the phase of the interferometric fringe spectrum and, therefore, can mimic dispersion. Similarly, it is possible to approximately compensate dispersion effects by using this scale parameter as an adjustable variable. This method of dispersion compensation has the limitation that it is depth dependent. Figure 10(b) shows a cross-sectional movie of the optic disk region acquired with unmatched dispersion. Dispersion was compensated by adjusting the bandwidth in the scale transformation. This image shows that the dispersion is compensated locally near the RPE, while other depths in the image are not compensated and have more resolution loss. In contrast, Fig. 10(a) shows that by using the numerical dispersion compensation procedure described in this paper, the dispersion is compensated at all depths. In these experiments the variable scale transformation bandwidth technique was used for approximate dispersion correction in the real-time display mode because it does not require any additional computation and can be performed at high speed.

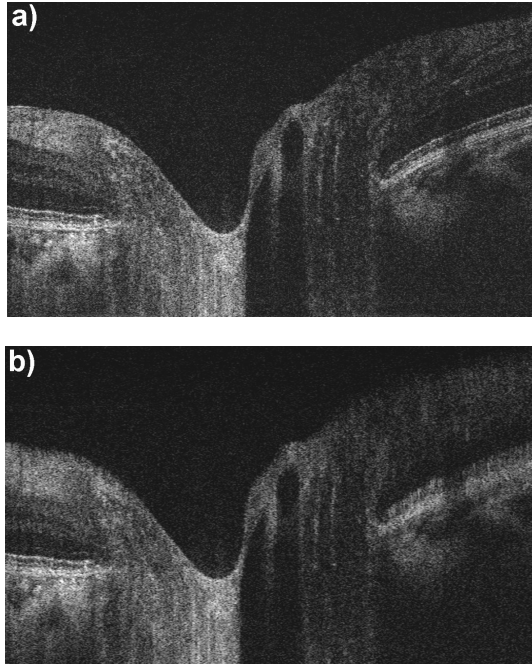


Fig. 10. a) (1.6 MB) High-speed spectral OCT movie of the optic disc with second- and third-order dispersion compensation using the automatic iterative method. b) (1.6 MB) High-speed spectral OCT movie of the optic disk with approximate dispersion compensation achieved by varying the scale or bandwidth parameter in the scale transformation. The movie in a) is sharp for all depths, while the movie in b) is dispersion compensated at only one depth. This is seen in the sharpening of the retinal pigment epithelium (RPE) on the left side of the image. These movies were acquired by using frames with 512 axial scans of 1024 pixels at a rate of 31 frames per second.

5. Discussion

This manuscript demonstrates ultrahigh-resolution spectral domain OCT. Using a broadband laser light source with FWHM = 144 nm, ultrahigh axial resolutions of up to $\sim 2.7 \mu\text{m}$ in air, corresponding to $\sim 2.1 \mu\text{m}$ in tissue, are achieved. The broad bandwidths used in ultrahigh-resolution OCT imaging necessitate special design of fiberoptic and optical components in the OCT system. Special attention is required to develop a spectrometer with broad bandwidth and high spectral resolution. The combination of the light source bandwidth, spectrometer bandwidth range, and CCD pixel number determine the axial resolution and scanning range.

A measured detection sensitivity of up to 98 dB is obtained by using an incident optical power of only 750 μW . The use of a 12-bit CCD line-scan camera enables a high dynamic range of 71 dB. Both axial resolution and sensitivity are very good, but axial resolution varies from $2.7 \mu\text{m}$ to $3.7 \mu\text{m}$, and sensitivity decreases from 98 dB to 80 dB across the axial measurement range of 1.4 mm. The reduction in sensitivity with axial delay is comparable to that reported in other studies using spectral domain OCT [17,22]. This means that only a portion of the axial measurement range has adequate sensitivity for high-performance imaging. Active tracking of the image axial position could improve performance, provided that the features being imaged have limited axial extent.

The performance of the ultrahigh-resolution spectral OCT system appears to be limited by the ability to build broad-bandwidth, high-resolution spectrometers. This problem is especially challenging because the spectrometer must detect the output of an optical fiber that emits light with a relatively large numerical aperture. In addition, the pixel size of current

CCD line-scan cameras is relatively small, in the range of 10 to 20 μm , thus requiring high numerical aperture focusing to a very small spot size at the output plane of the spectrometer. For our studies, the pixel size was 14 μm and the line-scan camera had 2048 pixels; resulting in a total width of \sim 28 mm. Thus, near-diffraction limit focusing must be maintained across a wide field of view on the spectrometer output plane. It is possible to improve the resolution per pixel by using line-scan cameras with larger numbers of pixels; however, this requires an even larger spectrometer field of view. Further attention to spectrometer design will be required to improve the decrease in sensitivity with delay that is seen in spectral OCT. It is interesting to note that degradation in sensitivity with axial delay should not be as pronounced in swept source OCT. There should be no significant loss of fringe contrast for high-frequency fringes compared to low-frequency fringes, provided that the linewidth of the light source is sufficiently narrow and the electronic detection bandwidth is sufficiently high.

Calibration of the spectrometer is also extremely important in maintaining resolution and in reducing the loss of sensitivity as a function of depth, because any error in the frequency calibration will result in a distortion of the interferometric fringe pattern. The 1200 line/mm grating spectrometer used in these studies was highly linear over a range of wavelengths in the source spectrum. However, any error in the linearity of the spectrometer can be corrected by the scale transformation, as shown in Fig. 1.

The broad bandwidths required to achieve ultrahigh-resolution OCT make dispersion matching between the sample and reference arms of the interferometer much more critical to achieving optimum resolution than in standard-resolution OCT. The numerical dispersion compensation method described in the manuscript performed as well as or better than physical matching of dispersion. This method also has the advantage that dispersion can be compensated to higher orders. Numerical dispersion compensation requires the use of an additional Hilbert transform and Fourier transform when compared to standard spectral OCT processing, which requires a single Fourier transform. A Hilbert transform is usually implemented by forward and reverse Fourier transforms. Thus, numerical dispersion compensation requires two additional Fourier transforms when compared to standard spectral OCT processing.

These results also demonstrate that automatic iterative algorithms may be applied which can optimize the dispersion compensation for an ultrahigh-resolution image. It is important to note that automatically compensating dispersion in an image, which has complicated backscattering and backreflections, is more challenging than for the case of a single reflection from a mirror. The automated iterative dispersion correction procedure presented here uses an image sharpness metric M , which minimizes the number of points above an empirically chosen threshold. If the threshold is set too high (e.g., near the peak signal value), the image sharpness may not be correctly optimized, because peaks are forced below the threshold in the process of maximizing the function M . If the threshold is set too low (e.g., near the noise level), the sharpness metric M does not have a well-defined maximum as the dispersion parameters are varied. For this study, the threshold was set to two standard deviations above the mean of the noise. This value of threshold worked well for retinal images from different subjects, and performance was not very sensitive to the specific threshold. With further investigation, other sharpness metrics can be developed.

The ability to automatically determine the parameters for dispersion compensation in an OCT image, and to numerically compensate the dispersion, promises to be especially important for ultrahigh-resolution ophthalmic imaging. In this case, eye length variations in the normal population or the absence of the lens in patients with cataract surgery can cause significant changes in dispersion that would degrade image resolution if uncompensated. As image resolutions are improved, broader bandwidths are required, thus making dispersion compensation progressively more important to achieving ultrahigh image resolutions. For very broad bandwidths and high resolutions, it would ultimately be necessary to compensate dispersion as a function of imaging depth. This can be accomplished by using more advanced numerical compensation techniques, such as dividing the axial range into multiple depth ranges and compensating dispersion for each depth range, or using wavelet decomposition

methods. Finally, since swept source OCT also provides direct access to the spectral fringes, all of the methods for numerical dispersion compensation and automatic iterative dispersion compensation presented here should apply to swept source OCT.

6. Conclusions

This study demonstrates ultrahigh-resolution, high-speed imaging using spectral domain OCT. Ultrahigh axial image resolutions of $\sim 2.1 \mu\text{m}$ in tissue are demonstrated. A 12-bit CCD linescan camera enables a dynamic range of 71 dB. Sensitivities of up to 98 dB using only 750 μW of incident power are achieved. Ultrahigh-resolution spectral domain OCT is shown to provide a $\sim 100\times$ increase in imaging speed when compared to ultrahigh-resolution time domain OCT. However, decrease in sensitivity with depth remains a limitation and additional development is required to solve this problem. Numerical dispersion compensation is demonstrated by constructing the complex representation of the spectral fringe pattern and correcting the phase as a function of frequency. This numerical method is shown to compensate relatively large dispersion mismatches. An iterative method was developed to automate the dispersion compensation procedure, yielding comparable or better image resolutions than could be obtained with physical dispersion matching. In conclusion, ultrahigh-resolution spectral domain OCT offers improved performance and versatility when compared to ultrahigh-resolution OCT using time domain detection.

Acknowledgments

We would like to acknowledge Aurea T. Zare for her assistance with the Ti:Sapphire laser. We also gratefully acknowledge scientific contributions and helpful advice from Desmond C. Adler, Robert Huber, Uwe Morgner, and Franz X. Kaertner. M. Wojtkowski is visiting from the Institute of Physics, Nicholas Copernicus University, Torun, Poland. This research was sponsored in part by National Institutes of Health R01-CA75289-06 and R01-EY11289-18, National Science Foundation ECS-01-19452 and BES-0119494, by the Air Force Office of Scientific Research Medical Free Electron Laser Program F49620-01-1-0186 and F49620-01-0084 and the Polish State Committee grant KBN 4T11E02322.